*Korean J. Chem. Eng.*, 39(5), 1268-1276 (2022)
DOI: 10.1007/s11814-021-1011-1

pISSN: 0256-1115
eISSN: 1975-7220

# Enhanced photocatalytic hydrogen evolution under visible light using noble metal-free ZnS NPs/Ni@Trimellitic acid porous microsphere heterojunction

**Wei-Qin Cai[*,**], Feng-Jun Zhang[*,**,†], Ying-Rui Wang[**,***], and Dong-Cai Li[**,†]**

*Key Laboratory of Functional Molecule Design and Interface Process, Anhui Jianzhu University, Hefei 230601, Anhui China
**Anhui Key Laboratory of Advanced Building Materials, Anhui Jianzhu University, Hefei 230601, Anhui China
***Construction Economy and Real Estate Management Research Center, Anhui Jianzhu University, Hefei 230601, Anhui China

(*Received 20 August 2021 • Revised 9 November 2021 • Accepted 10 November 2021*)

**Abstract**−The construction of late-model non-noble metal catalysts with above average performance and stability is the best choice to implement visible light decomposition of water for hydrogen production and solve the problem of clean energy. Herein, novel ZnS nanoparticles (ZnS NPs) grown in situ on the surface of porous Ni@Trimellitic acid (Ni-TA) microspheres were successfully synthesized. The structure, optical properties, element composition and others of ZnS/Ni-TA composites were systematically analyzed by experimental characterization. The experimental results showed that pure ZnS showed very weak photocatalytic performance. However, the photocatalytic performance was greatly increased with the addition of Ni-TA. The yield of the best sample (3% ZnS/Ni-TA) reached 1,098 μmol/g/h, about 12 times higher than that of ZnS. Among them, Ni-TA not only can be used as the main body of exotic metal nanoparticles, but also the porous channels can prevent the agglomeration of nanoparticles. The enhanced $H_2$ yield is mainly attributed to the resulting tight interface contact and well-matched band position which are conducive to effective carrier separation; moreover, the electrons quickly diverted to the exposed edge of Ni-TA for reducing to produce hydrogen. The combination of inorganic and new organic semiconductors provides an idea for hydrogen production under visible light.

Keywords: ZnS, Ni-TA, Porous Heterojunction, Visible Light Catalysis, Hydrogen Production

## INTRODUCTION

Hydrogen energy is the most promising green and clean energy in the 21st century [1,2]. Therefore, solar photocatalytic hydrolysis of hydrogen as a highly potential approach for sustainable development that has attracted widespread attention from researchers [3-5]. After in-depth research, scholars have found that transition metal sulfides are ideal semiconductor hydrogen production materials. Among them, zinc sulfide [6-8] (ZnS) has good semiconductor properties. It not only has high chemical stability and good electron mobility, but also has light corrosion resistance; especially, its reduction and oxidation charge potential is the very suitable photocatalytic decomposition of water [9,10]. These limitations result in a relatively short lifetime of photogenerated electrons, low quantum yield and solar energy conversion efficiency, which severely limits the photocatalytic hydrogen evolution performance of ZnS [11]. Therefore, to overcome the above-mentioned difficulties, many treatment methods have been carried out, such as morphology modulation and size change [12], adding promoters [13], combining with other semiconductors to form a heterojunction structure [14,15], and constructing a heterojunction composite material [16]. It also plays a vital role in improving the efficiency of photocatalysis.

Due to the good synergy between the various components of the inorganic-organic hybrid material, this provides a variety of possibilities for obtaining novel "intelligent" and excellent performance new materials. Inorganic-organic hybrid materials can not only preserve or improve the characteristics of each component, but also the synergy between them will produce new characteristics. Kim et al. [17] surveyed that the *in situ* polymerization of PDA on ZnS nanorods was achieved by precisely controlling the thickness of PDA layer. The strengthened photochemical catalysis competence was due to the type II band arrangement, which can effectively separate the charge and significantly reduce the ZnS band gap. The reduced oxidation capacity and high reduction potential of heterojunction nano catalysts confirmed the improvement of charge transfer in the composites. Soltani et al. [18] synthesized ZnS and CdS NPs coated for organic-inorganic substances under microwave irradiation, and obtained a novel catalyst with excellent photocatalytic competence. which coated nanoparticles were improved under visible light. Guo et al. [19] reported that ZnS was immobilized on PVDF particles by one-step phase transformation. The advantage of polymer carriers is that they can be made into various shapes by relatively simple methods. In addition, compared with inorganic substances, their low specific gravity increases the high dispersion in the reactor, which can promote light exposure and improve photocatalytic activity [20]. These reports have proved that the composite of organic-inorganic materials can improve photocatalytic activity. There is considerable literature about other organic semiconduc-

†To whom correspondence should be addressed.
E-mail: fjzhang@ahjzu.edu.cn, 2464934969@qq.com

tors compounding ZnS, but few reports on the application of trimellitic acid in the field of photocatalysis. Trimellitic acid is a kind of dissolved in artificial organic substance (NOM) with single bond COOH functional group [21]. Functional groups are in charge of dominating a number of significant properties and procedures, such as surfactant, sorption on metal surface, etc [22].

The development of high-efficiency, low-budget and stable visible light catalysts has straightforward been one of the principal study subjects [23]. In this work, the inorganic-organic ZnS/Ni-TA composite material has excellent hydrogen production performance, large pore size distribution, suitable energy band structure and stability, which are important factors for the introduction of TA. The unsaturated metal ions $Ni^{2+}$ atom dispersed in Ni-TA are used as the active center of the catalytic reaction. ZnS nanoparticles are grown *in situ* on the surface of Ni-TA by hydrothermal method to enhance the ability of electron transport. Ni-TA as an ideal carrier will hinder the accumulation of ZnS in the synthesis procedure, and the effecting close limiting surface touch and good match band position are conducive to effective carrier separation. This work paves the way for the further development of high-performance inorganic-organic semiconductor composite materials.

## EXPERIMENTAL

### 1. Materials

$NiCl_2 \cdot 6H_2O$, trimellitic acid, polyvinylpyrrolidone(PVP), absolute ethanol, methyl dimethylformate, $Zn(Ac)_2 \cdot 2H_2O$, $Na_2S \cdot 9H_2O$, $Na_2SO_3$ were purchased from Sinopharm Chemical Reagent Co., Ltd. Own reagents are analytically pure, no further purification is needed.

### 2. Synthesis of ZnS

Precipitation-hydrothermal method was used to prepare ZnS [24], Under vigorous stirring, 3.7 mmol of $Zn(Ac)_2 \cdot 2H_2O$ and 5.4 mmol of $Na_2S \cdot 9H_2O$ were added to 28.8 ml of deionized water and stirred for 60 min. The suspension was then shifted in a 473 K Teflon-lined stainless steel autoclave for 12 hours. The final product was centrifuged, cleaned with ethanol three times, then the specimen was put into a vacuum drying oven box and dried at 333 K for 10 hours.

### 3. Synthesis of Ni-TA and ZnS/Ni-TA

ZnS/Ni-TA composite was prepared by hydrothermal method, as indicated in Fig. 1. Usually, 0.864 g of $NiCl_2 \cdot 6H_2O$, 0.3 g of trimellitic acid and 3 g of PVP were added to a solvent mixed with 20 ml of deionized water, 20 ml of absolute ethanol and 20 ml of DMF, and stirred for 60 min. After sufficient stirring, the solution was shifted in a 473 K Teflon lined stainless steel autoclave for 10 hours. then naturally cooled to ambient temperature; the green solid material was cleaned several times with ethanol. The purpose was to remove the residual trimellitic acid. Finally, the sample was dried at 353 K for 10 h into an oven to obtain a Ni-TA material. The Ni-TA (1%, 3%, 5%, 7%) samples with different weight ratios were added to the ZnS synthesis step, denoted as 1% ZnS/Ni-TA, 3% ZnS/Ni-TA, 5% ZnS/Ni-TA, 7% ZnS/Ni-TA.

### 4. Photocatalysis for $H_2$ Production

At room temperature, photocatalytic hydrogen evolution experiments were performed by the photocatalytic hydrogen production evaluation system ((AuLight, Beijing, and CEL-SPH2N)). In the process of photocatalytic hydrogen production reaction, a 300 W Xe lamp was loaded with a cut-off filter ($\lambda$>420 nm) looked on as a visible light source. During the photocatalysis experiment, 0.02 g of photocatalyst and the sacrificial electron donors, $Na_2S \cdot 9H_2O$ (0.35 M)/$Na_2SO_3$ (0.25 M) were dispersed in 50 mL of deionized water using an ultrasonic bath for 15 min. Before the test, the system was degassed by a vacuum pump, and flowing circulating cooling water was generated by a low-temperature cooling circulating pump (CEL-CR300 (LX300)) to maintain the temperature of the reaction solution at 279 K. Keeping stirring continuously from first to last, the reaction was to avert the photocatalyst from agglomerating in the water. With $N_2$ as the carrier gas, a gas chromatograph (SP7800) equipped with a thermal conductivity detector (TCD) and 5 Å molecular sieve column was used to analyze the hydrogen generated under the 300 W AuLight (CEL-HXF300) simulated sunlight. See supporting information for AQE calculation [25-27]. The AQE of the sample was calculated according to Eq. (S1).

## RESULTS AND DISCUSSION

The phase structures of the ZnS, 3% ZnS/Ni-TA, and Ni-TA photocatalysts were determined by the powder XRD, as shown in Fig. 2. It can be clearly observed that the diffraction peaks at 9° and 12° are characteristic peaks of Ni-TA (Fig. 2(a)) [28]. For pure ZnS, four main characteristic peaks can be observed centered on 28.73°, 33.29°, 47.75° and 56.53°, which belong to the plane of (111), (200), (222) and (311), respectively. It can be well indexed as cubic ZnS sphalerite (JCPDS#05-0566) [8]. In Fig. 2(b), all composite materials show the same XRD trend as pure ZnS. In the

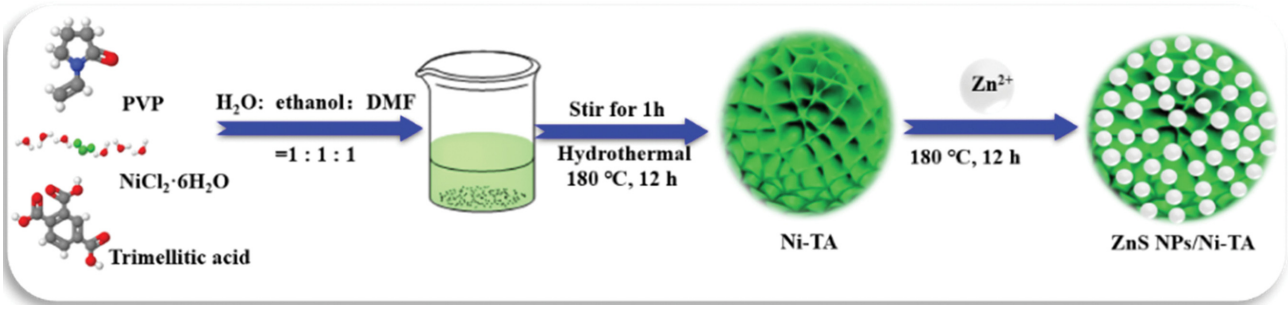


**Fig. 1. Preparation Process of ZnS/Ni-TA.**

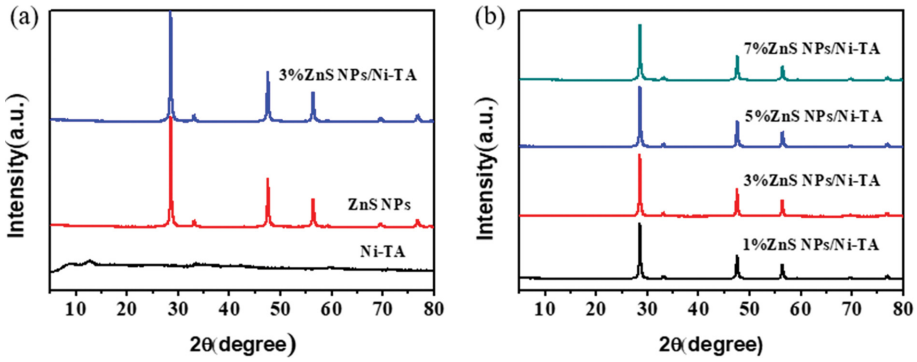


**Fig. 2. XRD patterns of (a) ZnS, 3% ZnS/Ni-TA, and Ni-TA; (b) ZnS/Ni-TA composite.**

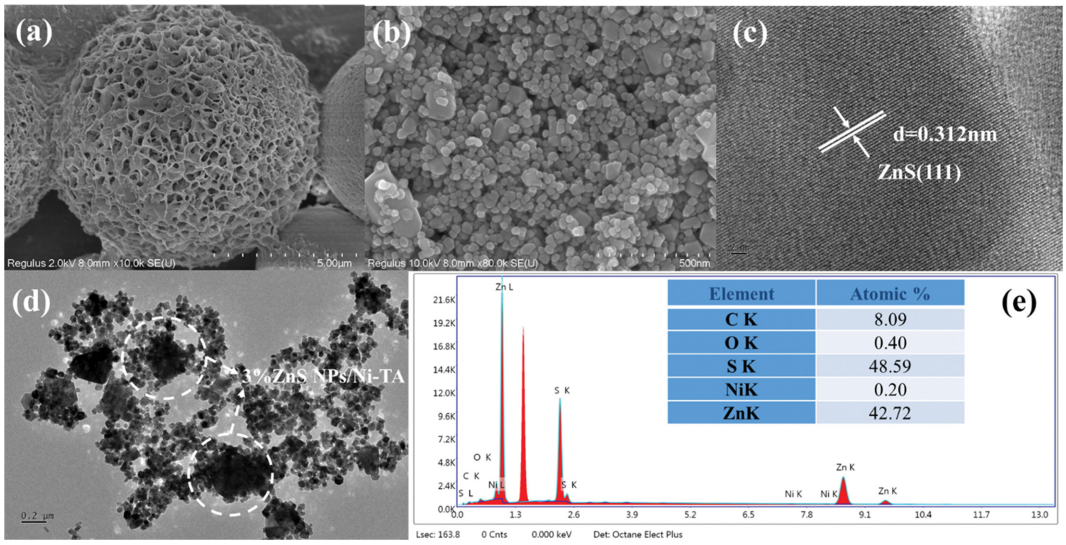


**Fig. 3. (a) SEM image of Ni-TA; (b)-(c) SEM and HRTEM image of ZnS; (d) TEM image of 3% ZnS/Ni-TA; (e) EDS image of 3% ZnS/Ni-TA.**

ZnS/Ni-TA photocatalyst, due to the low content of Ni-TA, the small diffraction intensity, and the diffraction peak of Ni-TA is covered by the strong diffraction peak of ZnS. To verify that Ni-TA has C, H, and O elements, after the successfully prepared Ni-TA is calcined at 873 K for 1 h, the sample completely becomes Ni O. Fig. S1 shows XRD of NiO, NiO exhibits three distinct diffraction peaks at 37.5°, 43.5°, and 63°, which correspond to (111), (200) and (220) crystal planes, respectively, and can be indexed as cubic NiO phase (JCPDS No. 47-1049), respecti vely [9,29,30]; the sample also has the original green to black.

Fig. 3(a), S2(a)-(b) shows the SEM images of Ni-TA with different sizes. It is obvious that Ni-TA presents a porous microsphere structure with relatively uniform size distribution in the range of 9-10 μm. SEM images of ZnS (Fig. 3(b)) show that the ZnS nanoparticles have uniform particle size. HRTEM image shows lattice fringes measured at 0.312 nm spacing, corresponding to the (111) plane of ZnS (JCPDS No. 05-0566) (Fig. 3(c)). In addition, no impurity peaks were observed. The TEM image of the 3% ZnS/Ni-TA composite (Fig. 3(d)) shows that ZnS nanoparticles cover the surface of Ni-TA. This close contact is conducive to the construction of heterojunction in 3% ZnS/Ni-TA composites, which is instrumental in the segregation of photoelectrons induced for ZnS, so it is conducive to the production of photocatalytic $H_2$. The results indicate that the successful mixing of porous spherical Ni-TA and ZnS can be deduced from the formation of 3% ZnS/Ni-TA heterojunction. Fig. 3(e), S2(c)-(i), exhibits elemental EDS and mapping of 3% ZnS/Ni-TA, which reflects the existence of elements in Zn, Ni, S, O and C. This is compatible with the outcome of TEM and SEM, indicating the formation for 3% ZnS/Ni-TA heterojunction.

The surface chemical composition and valence state of ZnS/Ni-TA were studied by X-ray photoelectron spectroscopy (XPS). The full-spectrum in Fig. 4(a) shows that the main elementary substances are Zn, S, Ni, O and C composition. No impurity substance peak was discovered in ZnS/Ni-TA composite material. The high-resolving power XPS spectra of Ni 2p, S 2p, Zn 2p and C 1s are in Fig. 4(b)-(d). The spectrum of Zn 2p is in Fig. 4(b). The binding energies of double strong peaks $2p_{3/2}$ and Zn $2p_{1/2}$ in the ZnS/Ni-TA composite are 1,021.8 and 1,044.8 eV, respectively, meaning the Zn elementary substance is in $Zn^{2+}$ chemical forms [8]. In addition, in the XPS spectrum of S 2p in Fig. 4(c), the peaks are deconvoluted into two peaks, showing that there are two peaks at

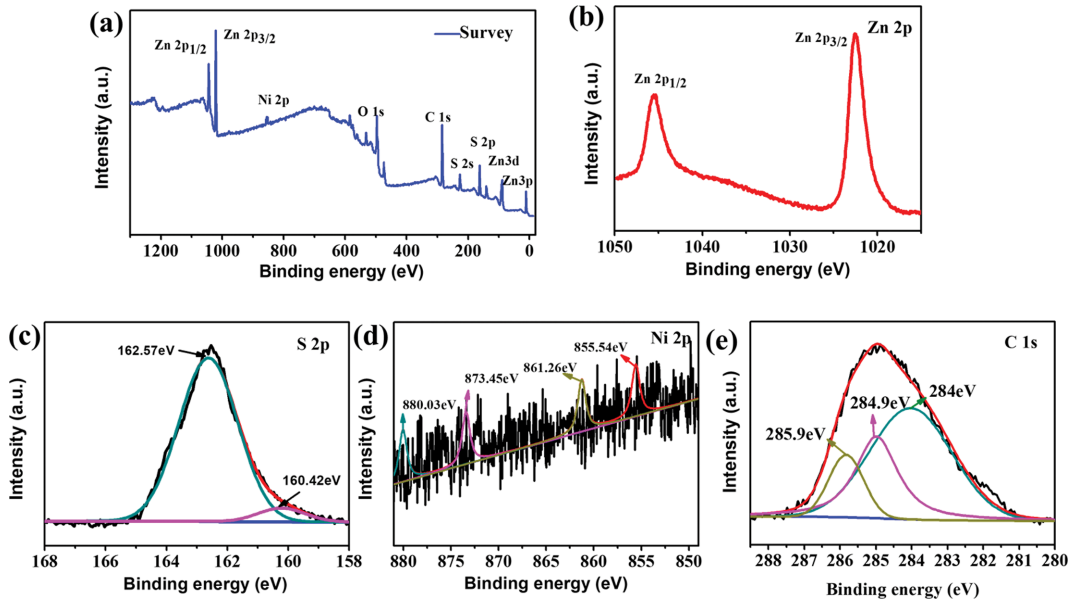


**Fig. 4. (a) XPS spectra of ZnS, Ni-TA, and ZnS/Ni-TA; (b) Zn 2p, (c) S 2p, (d) Ni 2p, (e) C 1s.**

160.42 and 162.57 eV, accounting for $2p_{1/2}$ and $2p_{3/2}$ for S 2p. These are typical characteristic peaks of $S^{2-}$, which are consistent with the reported spectra [7,31]. Similarly, Fig. 4(d) shows that the Ni-TA sample produces two pairs of peaks. The peaks at 855.59 and 873.04 eV correspond to Ni $2p_{1/2}$ and Ni $2p_{3/2}$, and the consisting satellite peaks correspond to 860.37 and 879.92 eV [32,33]. The C 1s peak of 3% ZnS/Ni-TA sample can be deconvoluted into three peaks centered at 284 eV, 284.9 eV and 285.9 eV, corresponding to the C-C/C=C ($sp^2$ carbon), C-C, and C-O bonds, respectively (Fig. 4(e)) [34]. XPS results confirmed the successful combination of Ni-TA and ZnS in the 3% ZnS/Ni-TA binary composite. XPS can be used for quantitative analysis of elements. The content or relative concentration of reaction atoms according to the photoelectron line intensity (area of photoelectron peak) in the energy spectrum. XPS atomic concentration (%) of 3% ZnS/Ni-TA is shown in the Table S1. The result can imply the formation of ZnS/Ni-TA heterojunction.

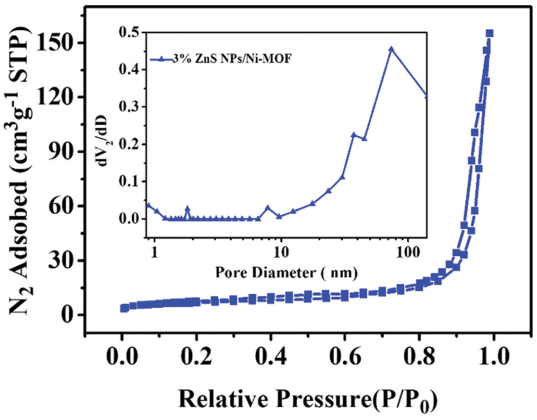


**Fig. 5. $N_2$ adsorption-desorption isotherms and pore size distribution of ZnS/Ni-TA.**

It can be clearly seen in Fig. 5 that the adsorption and desorption curves of the samples do not overlap. The adsorption rate of the sample increases gradually with the increase of pressure, and in the higher $P/P_0$ region (0.8-1.0), the isotherm rises rapidly due to the capillary condensation of the adsorbent [35,36]. Moreover, when all the pores are clustered together, adsorption occurs mainly on the outer surface, which is much smaller than the inner surface area, so the curve is flat. When $P/P_0$ reaches 1.0, adsorption occurs on the macropore and the curve rises. According to the IUPAC classification, obviously, ZnS/Ni-TA follows the type IV isotherm with H3 hysteresis loops, indicating the presence of mesopores in the photocatalyst [37,38]. After hydrothermal reaction, the composite forms a porous spherical structure with large pore size; this result is in good agreement with the SEM analysis. The specific surface area is 19.765 $m^2/g$ and the total pore volume is 0.291 cc/g.

The optical performance for ZnS, Ni-TA and ZnS/Ni-TA composite materials was studied by ultraviolet-visible diffuse reflectance spectroscopy (Fig. 6(a)). The specific surface area (BET) and pore structure of produces were investigated by the $N_2$ adsorption-desorption test at 77 K. For the ZnS/Ni-TA (X) photocatalyst, as the content of Ni-TA increases, the site of the absorption edge gradually shifts into visible light, which is beneficial for photocatalytic HER activity. The red shift of optical absorption is correlated with the inherent visible light response for ZnS. The analysis further confirms the composition of the two components into the composite material meets the requirements, which is the cause of $H_2$ driven by visible light. According to Tauc's equation, $\alpha h\nu = A(h\nu - E_g)^{n/2}$, the band gap energy is calculated from the measurement curve by fitting, where A is a constant independent of $h\nu$, $E_g$ is the semiconductor band gap, and n depends on the transition type. Similarly, the semiconductor band gap energy is determined according to the intersection of the linear fit of $(\alpha h\nu)^{1/n}$ and $h\nu$ on the x-axis. For direct and indirect band gaps, n is 1/2 and 2,

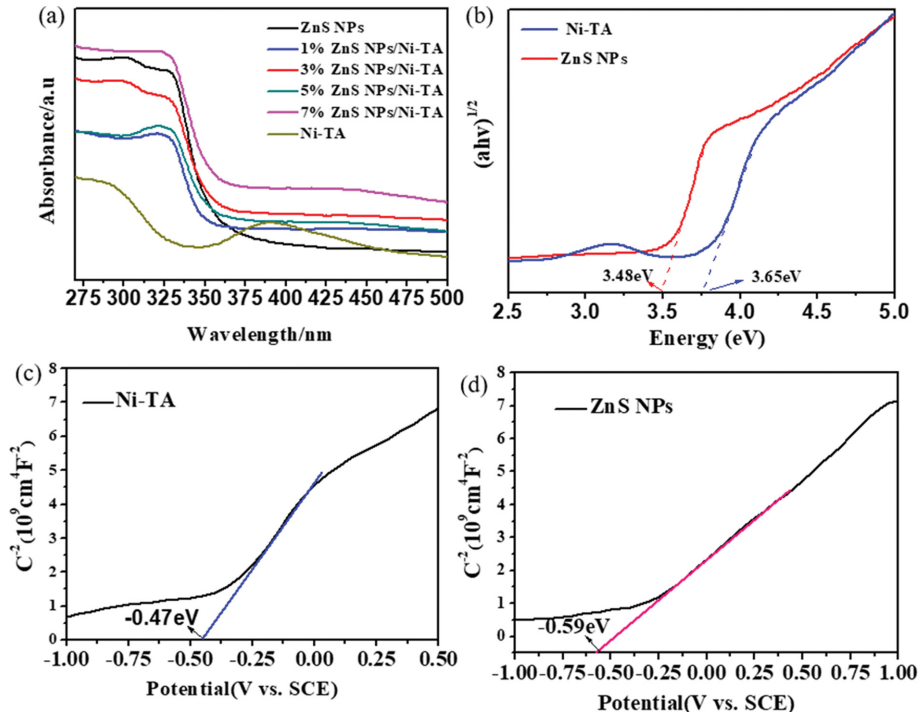


**Fig. 6. (a) UV-vis absorption spectra, (b) Tauc plots and (c)-(d) Mott-Schottky plots of ZnS, Ni-TA, and ZnS/Ni-TA(X).**

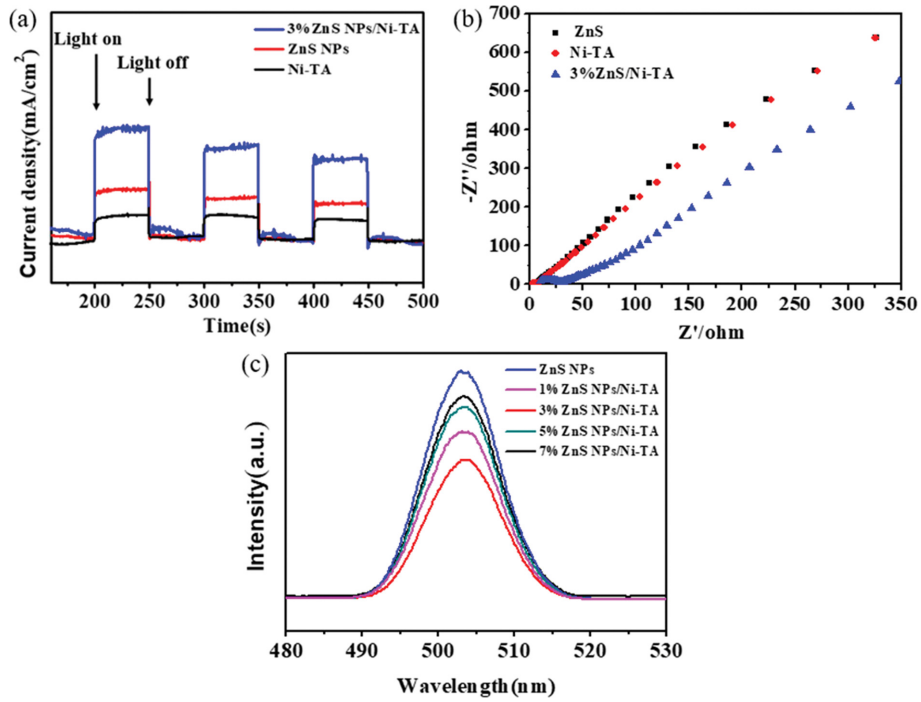


**Fig. 7. (a) Transient photocurrent response, (b) EIS impedance plot, and (c) PL emission spectra of ZnS, Ni-TA, and ZnS/Ni-TA(X).**

respectively. The calculated band gaps of ZnS and Ni-TA are 3.48, 3.65, respectively (Fig. 6(b)). The sites of VB and CB have decisive great effects on the direction of separation and shift to $e^-$-$h^+$ pairs. For this purpose, the Mott-Schottky study of ZnS nanoparticles and Ni-TA was carried out to research the electronic energy band structures (Fig. 6(c)-(d)). Note that it has the characteristics of n-type semiconductors [39]. On the basis of the x-intercept in the M-S map, the potential of the $E_{CB}$ can be roughly evaluated.

The calculated $E_{CB}$ values of ZnS nanoparticles and Ni-TA are –0.59 eV and –0.47 eV, respectively. Combining the Kubelka-Munk

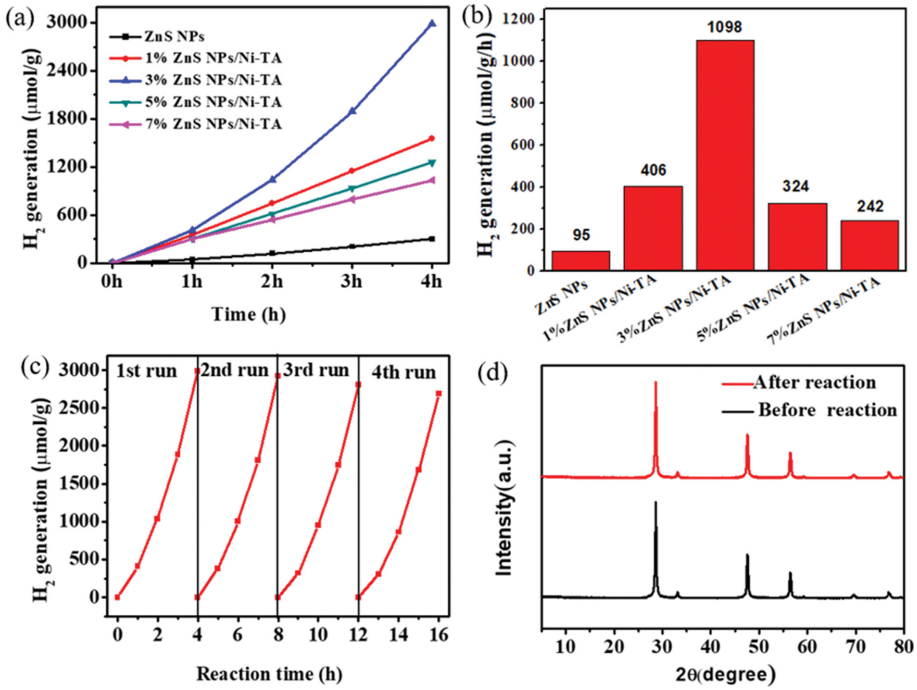


**Fig. 8. (a)-(b) Photocatalytic $H_2$ evolution of ZnS, Ni-TA, and ZnS/Ni-TA(X). (c) Recycle test (4 cycles) of photocatalytic $H_2$ evolution over 3%ZnS/Ni-TA. (d) XRD patterns of the before and after 3%ZnS/Ni-TA.**

function $(\alpha h\nu)^{1/n}$ and the graph of the absorbed light energy switched from the UV-visible spectroscopy, it can be inferred that the $E_{VB}$ of ZnS nanoparticles and Ni-TA are 2.89 and 3.18 eV separately. It turns out to be the case that the CB of ZnS is higher than that of Ni-TA. When the ZnS nanomaterial is excited through an external illuminant, the photo-generated $e^-$-$h^+$ pairs can recombine without difficulty, radiate energy by a fluorescent pattern so that reach a steady-state, thus indirectly verifying the photocatalytic property.

Electrochemical impedance spectroscopy (EIS) and photocurrent response are important factors in evaluating the productivity of photoinduced charge excellent separation efficiency and efficient mass transfer performance [3,40]. In an electrochemical measurement, Fig. 7(a) demonstrates a graph of the transient photocurrent response. It can be seen that the ZnS/Ni-TA composite has favorable photoelectrochemical performance and repeatability, However, the photocurrent response of ZnS is exceedingly small. When added with Ni-TA, its photocurrent density increases due to valid charge shift, boosting charge part and reducing recombination proportion [41]. It turns out that the heterojunction formed through ZnS and ZnS/Ni-TA improves its photoelectrochemical performance and fundamentally reduces the recombination petty of photogenerated $e^-$-$h^+$. At that precise moment, Ni-TA acts as the electron transfer gathering place and reaction promoter of ZnS. As shown in Fig. 7(b), the radius of curvature of the ZnS/Ni-TA composite is the smallest, representing the minimum charge-transfer obstruction and indicating that the ZnS/Ni-TA composite has a faster face $e^-$ mobility to accomplish effective carrier segregation [42]. The carrier transport path influences the photocatalytic performance as well and this conclusion is consistent with the results of photocatalytic hydrogen production. Under excitation at a fixed wavelength (Fig. 7(c)), ZnS nanoparticles exhibit higher PL emission intensity due to the easy carrier recombination on ZnS. When ZnS adheres to the surface of Ni-TA, the fluorescence intensity is efficaciously eliminated, which proves that there is a strong interaction between ZnS and Ni-TA. The results show that the photogenerated electrons of ZnS are quickly shifted into Ni-TA, which increases the rapid segregation of photo-generated $e^-$-$h^+$ pairs and enhances the photocatalytic $H_2$ evolution performance of the composite material.

Under visible light ($\lambda$>420 nm), $Na_2S$ and $Na_2SO_3$ are used as hole sacrificial reagents, and the $H_2$ generated by photocatalytic water splitting would assess the activity of the prepared samples. Fig. 8(a) shows that the $H_2$ production proportion of the ZnS/Ni-TA composite is that of ZnS, illustrating that the porous structure helps to enhance the performance of photocatalytic $H_2$ production. Due to the inherent shortcomings of pure ZnS, its hydrogen production rate under visible light irradiation is exceedingly small (95 $\mu molg^{-1}h^{-1}$). The hydrogen production rate increased significantly after adding Ni-TA. The highest hydrogen production rate of 3% ZnS/Ni-TA (1,098 $\mu molg^{-1}h^{-1}$) is about 12 times that of pure ZnS nanoparticles, indicating that Ni-TA is more beneficial as a co-catalyst photocatalytic hydrogen evolution. In addition, the photocatalytic hydrogen production performance of Ni-TA with different loadings was studied (Fig. 8(b)). It increases linearly with the increase of Ni-TA content, because the number of reducing active sites increases. However, a further increase in the content of Ni-TA will result in a gradual decrease in photocatalytic performance. This is because in the case of lower Ni-TA content, although the number of photogenerated electrons and holes is sufficient, the

**Table 1. Performance comparison of different ZnS based photocatalysts**

| No. | Photocatalyst | Light source | Photocatalytic $H_2$ evolution rate | Sacrificial agent | Reference |
|---|---|---|---|---|---|
| 1 | ZnS/Ni-TA | Visible light | 1,098 $\mu mol \cdot h^{-1} \cdot g^{-1}$ | $Na_2S/Na_2SO_3$ (0.25 M/0.35 M) | This work |
| 2 | CdS-ZnS core-shell particles | Visible light | 792 $\mu mol \cdot h^{-1} \cdot g^{-1}$ | $Na_2S/Na_2SO_3$ | [43] |
| 3 | Porous ZnS : $Ag_2S$ nanosheets | Visible light | 104.9 $\mu mol \cdot h^{-1} \cdot g^{-1}$ | $Na_2S/Na_2SO_3$ (0.1 M/0.1 M) | [44] |
| 4 | C-doped ZnS-ZnO/Rh | Visible light | 806 $\mu mol \cdot h^{-1} \cdot g^{-1}$ | $Na_2S/Na_2SO_3$ | [45] |
| 5 | $Cu_2ZnSnS_4$/ZnS | Visible light | 432 $\mu mol \cdot h^{-1} \cdot g^{-1}$ | $Na_2S/Na_2SO_3$ (0.1 M/0.1 M) | [46] |
| 6 | CuS/ZnS | Visible light | 695.7 $\mu mol \cdot h^{-1} \cdot g^{-1}$ | $Na_2S/Na_2SO_3$ (0.35 M/0.25 M) | [47] |
| 7 | Ni-P/defect-rich ZnS | Visible light | 69.92 $\mu mol \cdot h^{-1} \cdot g^{-1}$ | $Na_2S/Na_2SO_3$ (0.1 M/0.1 M) | [48] |
| 8 | Pt/ZnS-ZnO | Visible light | 121.8 $\mu mol \cdot h^{-1} \cdot g^{-1}$ | $Na_2S/Na_2SO_3$ (0.1 M/0.1 M) | [49] |
| 9 | $Zn_{1-x}Cd_xS$/D-ZnS(en)$_{0.5}$ | Visible light | 463.6 $\mu mol \cdot h^{-1} \cdot g^{-1}$ | $Na_2S/Na_2SO_3$ (0.35 M/0.25 M) | [50] |
| 10 | flower-like ZnO@ZnS | Visible light | 126.2 $\mu mol \cdot h^{-1} \cdot g^{-1}$ | Methanol (10 vol%) | [51] |

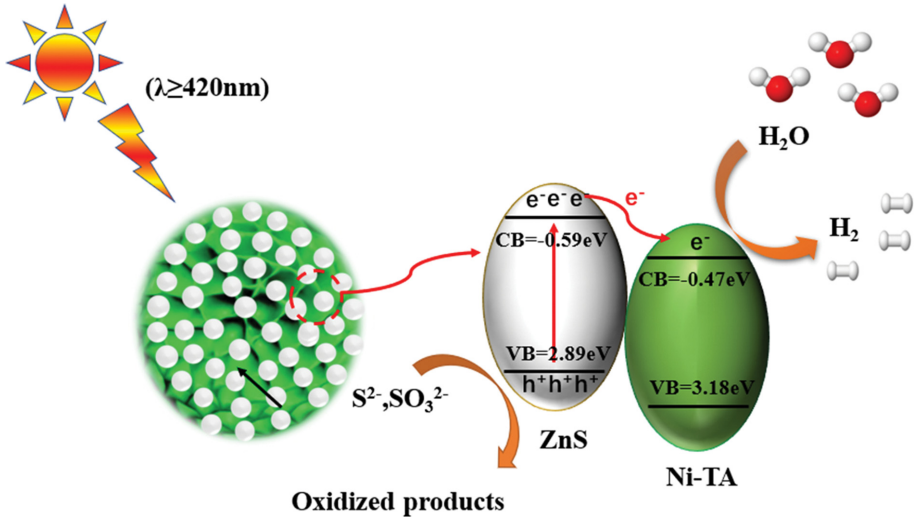


**Fig. 9. Proposed photocatalytic mechanism of photocatalytic hydrogen evolution of ZnS/Ni-TA.**

lack of Ni-TA cannot effectively inhibit photogenerated electron-hole recombination. However, too much Ni-TA will form aggregation, resulting in a decrease in surface area and blocking light from entering. Therefore, controlling the ratio of Ni-TA to ZnS is the key to achieving the best photocatalytic activity of ZnS/Ni-TA composites. Therefore, when the mass ratio of Ni-TA to ZnS is 3%, 3% ZnS/Ni-TA has the best photocatalytic hydrogen production activity, and the hydrogen generation rate is as high as 1,098 $\mu molg^{-1}h^{-1}$. The AQE of 3% ZnS/Ni-TA is 15.5%. This is due to the good dispersion of ZnS on the Ni-TA surface, which can capture more light and generate more light-excited electrons. Stability is an important factor affecting the photocatalytic performance. We further measured the hydrogen production of the 3% ZnS/Ni-TA composite material for 16 h continuously over time (Fig. 8(c)). It can be concluded from Table 1 that the activity of ZnS/Ni-TA photocatalyst for solar water decomposition is better than that of ZnS photocatalyst modified by some cocatalysts previously reported. With the prolongation of the illumination time, the amount of hydrogen produced linearly increases. As shown in Fig. 8(c), the hydrogen production volume of the second cycle, the third cycle and the fourth cycle is similar to the hydrogen production volume of the first cycle, indicating that the material prepared has great cycle stability. Comparing the XRD spectra of the 3% ZnS/Ni-TA composite before and after the four cycles of $H_2$ precipitation (Fig. 8(d)) shows that after long-term $H_2$ precipitation, the crystal structure of the sample does not change significantly. These results well show that the comparative 3% ZnS/Ni-TA composite has high performance and stable photocatalytic hydrogen evolution performance.

Fig. 9 shows the probable photocatalytic reaction mechanism of ZnS/Ni-TA composite on the basis of all the characterization conclusions before. Under visible light irradiation, ZnS generates $e^-$-$h^+$ pairs, and the electrons on the CB through a reduction reaction generate $H_2$, yet the $e^-$-$h^+$ pairs quickly recombine, leading to poor photocatalytic $H_2$ evolution efficiency. When ZnS is loaded on the surface of Ni-TA, the two form a heterojunction structure. The electrons excited by the ZnS nanoparticles are rapidly shifted to the uncovered edge of Ni-TA for reduction to generate hydrogen gas, which is instrumental in the effective segregation of $e^-$-$h^+$ pairs. The photo-generated holes in the ZnS valence band react with hole sacrificial agents ($Na_2S$ and $Na_2SO_3$) to form their oxidation products. The transfer of electrons and the consumption of photo-generated holes inhibit charge recombination, enhance the chemical stability of the complex, and help improve the photocata-

lytic $H_2$ production performance. This work paves the way for the further development of high-performance inorganic-organic semiconductor composite materials.

## CONCLUSIONS

ZnS nanoparticles were grown *in situ* on the surface of Ni-TA by hydrothermal method. The results show that under visible light irradiation, with $Na_2S$ and $Na_2SO_3$ as sacrificial reagents, the $H_2$ release rate of the ZnS/Ni-TA composite is as high as 1,098 $\mu molg^{-1} h^{-1}$, which is about 12 times higher than that of ZnS (95 $\mu molg^{-1} h^{-1}$) . Because the CB of ZnS and the LUMO of Ni-TA have suitable positions, electrons can be transferred directionally, thus reducing the recombination of $e^-$-$h^+$ in ZnS nanoparticles, thereby realizing photo-induced charge separation. In addition, Ni-TA not only plays a vital role in fundamentally capturing the charge generated by light in ZnS, but also provides $Ni^{2+}$ catalytic centers. The high dispersibility of $Ni^{2+}$ enables the catalyst to have great steadiness over a long period of time reaction, and overcomes the problem that noble metal nanoparticle catalysts usually affect their catalytic availably and stability. This work provides a new way to construct efficacious and stable precious metal-free organic-inorganic semiconductor catalysts.

## ACKNOWLEDGEMENTS

This work was financially supported by the Major Projects of Natural Science Research in Anhui Colleges and Universities (KJ2018ZD050, GXXT-2019-017, GXXT-2020-009), Natural Science Foundation of Anhui province (1808085ME129), Key research and development plan of Anhui Province (202004a05020060), Outstanding Young Talents Support Program in Colleges and Universities (gxyqZD2018056).

## SUPPORTING INFORMATION

Additional information as noted in the text. This information is available via the Internet at http://www.springer.com/chemistry/journal/11814.

## REFERENCES

1. H. Che, C. Li, P. Zhou, C. Liu, H. Dong and C. Li, *Appl. Surf. Sci.*, **505**, 144564 (2020).
2. R. Chen, P. Wang, J. Chen, C. Wang and Y. Ao, *Appl. Surf. Sci.*, **473**, 11 (2019).
3. R. K. Chava, J. Y. Do and M. Kang, *Appl. Surf. Sci.*, **433**, 240 (2018).
4. P. Jin, L. Wang, X. Ma, R. Lian, J. Huang, H. She, M. Zhang and Q. Wang, *Appl. Catal. B: Environ.*, **284**, 119762 (2021).
5. A. Kumar, M. Kumar, V. Navakoteswara Rao, M. V. Shankar, S. Bhattacharya and V. Krishnan, *J. Mater. Chem. A*, **9**, 17006 (2021).
6. Y. Feng, M. Xu, P.-L. Tremblay and T. Zhang, *Int. J. Hydrogen Energy*, **46**, 21901 (2021).
7. M. Jing, Z. Chen, Z. Li, F. Li, M. Chen, M. Zhou, B. He, L. Chen, Z. Hou and X. Chen, *ACS Appl. Mater. Interfaces*, **10**, 704 (2018).
8. R. Rameshbabu, P. Ravi and M. Sathish, *Chem. Eng. J.*, **360**, 1277 (2019).
9. V. Navakoteswara Rao, P. Ravi, M. Sathish, N. Lakshmana Reddy, K. Lee, M. Sakar, P. Prathap, M. Mamatha Kumari, K. Raghava Reddy, M. N. Nadagouda, T. M. Aminabhavi and M. V. Shankar, *J. Hazard. Mater.*, **413**, 125359 (2021).
10. S. Kumar, N. L. Reddy, H. S. Kushwaha, A. Kumar, M. V. Shankar, K. Bhattacharyya and V. Krishnan, *ChemSusChem*, **10**, 3588 (2017).
11. D. Ramírez-Ortega, A. B. Ramos, A. Hernández-Gordillo, R. Zanella and S. E. Rodil, *Int. J. Hydrogen Energy*, **45**, 30496 (2020).
12. Y. Hong, J. Zhang, F. Huang, J. Zhang, X. Wang, Z. Wu, Z. Lin and J. Yu, *J. Mater. Chem. A*, **3**, 13913 (2015).
13. R. Rameshbabu, P. Ravi, G. Pecchi, E. J. Delgado, R. V. Mangalaraja and M. Sathish, *J. Colloid Interface Sci.*, **590**, 82 (2021).
14. S. Dhingra, T. Chhabra, V. Krishnan and C. M. Nagaraja, *ACS Appl. Ener. Mater.*, **3**, 7138 (2020).
15. A. Kumar, V. N. Rao, A. Kumar, M. V. Shankar and V. Krishnan, *ChemPhotoChem*, **4**, 427 (2020).
16. S. Kumar, A. Kumar, V. Navakoteswara Rao, A. Kumar, M. V. Shankar and V. Krishnan, *ACS Appl. Ener. Mater.*, **2**, 5622 (2019).
17. Y. Kim, E. Coy, H. Kim, R. Mrówczyński, P. Torruella, D.-W. Jeong, K. S. Choi, J. H. Jang, M. Y. Song, D.-J. Jang, F. Peiro, S. Jurga and H. J. Kim, *Appl. Catal. B: Environ.*, **280**, 119423 (2021).
18. N. Soltani, E. Saion, W. M. M. Yunus, M. Erfani, M. Navasery, G. Bahmanrokh and K. Rezaee, *Appl. Surf. Sci.*, **290**, 440 (2014).
19. J. Guo, S. Khan, S.-H. Cho and J. Kim, *Appl. Surf. Sci.*, **473**, 425 (2019).
20. A. Y. Shan, T. I. M. Ghazi and S. A. Rashid, *Appl. Catal. A-Gen.*, **389**, 1 (2010).
21. R. Rangsivek and M. R. Jekel, *Chemosphere*, **71**, 18 (2008).
22. H. Gocmez, *Ceram. Int.*, **32**, 521 (2006).
23. N. Subha, M. Mahalakshmi, S. Monika and B. Neppolian, *Int. J. Hydrogen Energy*, **45**, 7552 (2020).
24. C. Zhang, Y. Zhou, J. Bao, J. Fang, S. Zhao, Y. Zhang, X. Sheng and W. Chen, *Chem. Eng. J.*, **346**, 226 (2018).
25. A. Kumar, A. Kumar and V. Krishnan, *ACS Catalysis*, **10**, 10253 (2020).
26. A. Kumar, V. Navakoteswara Rao, A. Kumar, A. Mushtaq, L. Sharma, A. Halder and V. Krishnan, *ACS Appl. Ener. Mater.*, **3**, 12134 (2020).
27. A. Kumar and V. Krishnan, *Adv. Funct. Mater.*, **31**, 2009807 (2021).
28. F. Zou, Y. M. Chen, K. Liu, Z. Yu, W. Liang, S. M. Bhaway, M. Gao and Y. Zhu, *ACS Nano*, **10**, 377 (2016).
29. J. Wang, Y. Liu, Z. Wang, P. Wang, Z. Zheng, X. Qin, X. Zhang, Y. Dai and B. Huang, *Int. J. Hydrogen Energy*, **44**, 16575 (2019).
30. N. Chen, J. Cao, M. Guo, C. Liu, H. Lin and S. Chen, *Int. J. Hydrogen Energy*, **46**, 19363 (2021).
31. X. Wang, G. Li, F. M. Hassan, J. Li, X. Fan, R. Batmaz, X. Xiao and Z. Chen, *Nano Energy*, **15**, 746 (2015).
32. Q. Zhou, Y. Gong and K. Tao, *Electrochim. Acta*, **320**, 134582 (2019).
33. J. Ran, J. Qu, H. Zhang, T. Wen, H. Wang, S. Chen, L. Song, X. Zhang, L. Jing, R. Zheng and S. Z. Qiao, *Adv. Energy Mater.*, **9**, 1803402 (2019).
34. H. Sun, Y. Lian, C. Yang, L. Xiong, P. Qi, Q. Mu, X. Zhao, J. Guo, Z. Deng and Y. Peng, *Energy Environ. Sci.*, **11**, 2363 (2018).
35. X. Yan and Z. Jin, *Chem. Eng. J.*, **420**, 127682 (2020).
36. T. Liu, K. Yang and Z. Jin, *Mol. Catal.*, **510**, 111691 (2021).
37. B. Shao, Z. Liu, G. Zeng, Z. Wu, Y. Liu, M. Cheng, M. Chen, Y.

Liu, W. Zhang and H. Feng, *ACS Sustain. Chem. Eng.*, **6**, 16424 (2018).
38. B. Shao, X. Liu, Z. Liu, G. Zeng, W. Zhang, Q. Liang, Y. Liu, Q. He, X. Yuan, D. Wang, S. Luo and S. Gong, *Chem. Eng. J.*, **374**, 479 (2019).
39. J. Guo, Y. Liang, L. Liu, J. Hu, H. Wang, W. An and W. Cui, *Appl. Surf. Sci.*, **522**, 146356 (2020).
40. G. Chen, D. Li, F. Li, Y. Fan, H. Zhao, Y. Luo, R. Yu and Q. Meng, *Appl. Catal. A: Gen.*, **443**, 138 (2012).
41. A. Hassan, R. Liaquat, N. Iqbal, G. Ali, X. Fan, Z. Hu, M. Anwar and A. Ahmad, *J. Electroanal. Chem.*, **889**, 115223 (2021).
42. L.-L. Chu, *Catal. Commun.*, **128**, 105705 (2019).
43. Y. P. Xie, Z. B. Yu, G. Liu, X. L. Ma and H.-M. Cheng, *Energy Environ. Sci.*, **7**, 1895 (2014).
44. X. Yang, H. Xue, J. Xu, X. Huang, J. Zhang, Y. B. Tang, T. W. Ng, H. L. Kwong, X. M. Meng and C. S. Lee, *ACS Appl. Mater. Interfaces*, **6**, 9078 (2014).
45. S. Khan, M. Je, N. N. T. Ton, W. Lei, T. Taniike, S. Yanagida, D. Ogawa, N. Suzuki, C. Terashima, A. Fujishima, H. Choi and K.-i. Katsumata, *Appl. Catal. B: Environ.*, **297**, 120473 (2021).
46. F. Jiang, B. Pan, D. You, Y. Zhou, X. Wang and W. Su, *Catal. Commun.*, **85**, 39 (2016).
47. L. Xiao, H. Chen and J. Huang, *Mater. Res. Bull.*, **64**, 370 (2015).
48. S. Zhu, X. Qian, D. Lan, Z. Yu, X. Wang and W. Su, *Appl. Catal. B: Environ.*, **269**, 118806 (2020).
49. X. Wang, Z. Cao, Y. Zhang, H. Xu, S. Cao and R. Zhang, *Chem. Eng. J.*, **385**, 123782 (2020).
50. W. Feng, Y. Wang, X. Huang, K. Wang, F. Gao, Y. Zhao, B. Wang, L. Zhang and P. Liu, *Appl. Catal. B: Environ.*, **220**, 324 (2018).
51. X. Yang, H. Liu, T. Li, B. Huang, W. Hu, Z. Jiang, J. Chen and Q. Niu, *Int. J. Hydrogen Energy*, **45**, 26967 (2020).

# Supporting Information

# Enhanced photocatalytic hydrogen evolution under visible light using noble metal-free ZnS NPs/Ni@Trimellitic acid porous microsphere heterojunction

**Wei-Qin Cai[*,**], Feng-Jun Zhang[*,**,†], Ying-Rui Wang[**,***], and Dong-Cai Li[**,†]**

*Key Laboratory of Functional Molecule Design and Interface Process, Anhui Jianzhu University, Hefei 230601, Anhui China
**Anhui Key Laboratory of Advanced Building Materials, Anhui Jianzhu University, Hefei 230601, Anhui China
***Construction Economy and Real Estate Management Research Center, Anhui Jianzhu University, Hefei 230601, Anhui China
(*Received 20 August 2021 • Revised 9 November 2021 • Accepted 10 November 2021*)

## S1. Characterization

Take copper K$\alpha$ radiation ($\lambda$=1.5406) as the radiation source, and record the X-ray diffraction pattern with the Bruker D8 advanced diffractometer, the scanning range is 5-80 degrees. The catalyst was studied by scanning electron microscope (Joel, JSM-7500), transmission electron microscope (JEM-2100) and high resolution transmission electron microscope (HRTEM) for the surface micro morphology. The optical properties of the catalyst were studied with an ultraviolet-visible diffuse reflectance spectrometer (SolidSpec-3700), and barium sulfate was used as a standard reference material. XPS (Thermo Fisher Scientific K-Alpha) characterizations were conducted by Suqian Ning-biao Technical Testing Co., Ltd. The photoluminescence spectrum was tested by a fluorescence spectrometer (Japanese) at an excitation wavelength of 320 nm using photoluminescence spectroscopy. In the photoelectrochemical measurement, the photoelectrochemical measurement of the photoelectric properties of the sample was tested with a standard three-electrode system on an electro-chemical workstation (Brilliance) using sodium sulfate solution as the electrolyte.

## AQE Calculation

The 3% ZnS/Ni-TA was irradiated by a 300 W Xe lamp for 4 h. The irradiation area was 10.9 $cm^2$. The average amount of hydrogen production in 4 h for 3% ZnS/Ni-TA was 84.98 μmol. The apparent quantum efficiency (AQE) of the sample was calculated according to Eq. (S1) [25-27].

Number of incident photons:

$$N=\frac{E\lambda}{hc}=\frac{10.9\times80\times10^{-3}\times3600\times420\times10^{-9}}{6.626\times10^{-34}\times3\times10^{8}}=6.63\times10^{21}$$

$$AQE=\frac{2\times\text{amount of } H_2 \text{ molecules evolved in unit time}}{\text{number of incident photons in unit time}}\times100\%$$

$$=\frac{2\times6.02\times10^{23}\times84.98\times10^{-6}}{6.61\times10^{21}}\times100\%=15.5\%$$

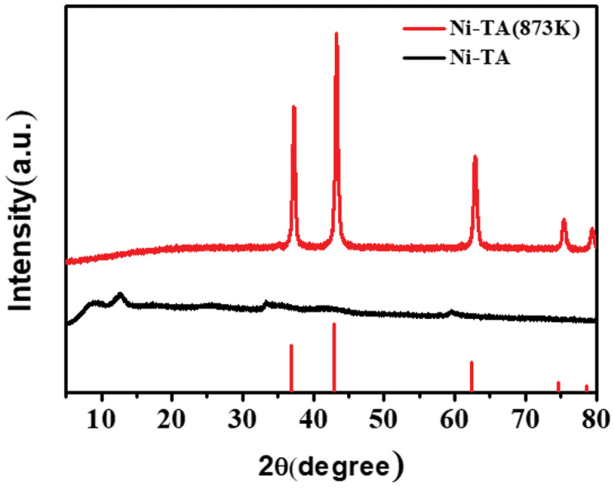


**Fig. S1. XRD patterns of Ni-TA and Ni-TA (873 K).**

**Table S1. XPS atomic concentration (%) of 3% ZnS/Ni-TA**

| Name | Atomic % |
|---|---|
| C 1s | 72.89 |
| S 2p | 13.93 |
| Zn 2p | 12.44 |
| Ni 2p | 0.75 |

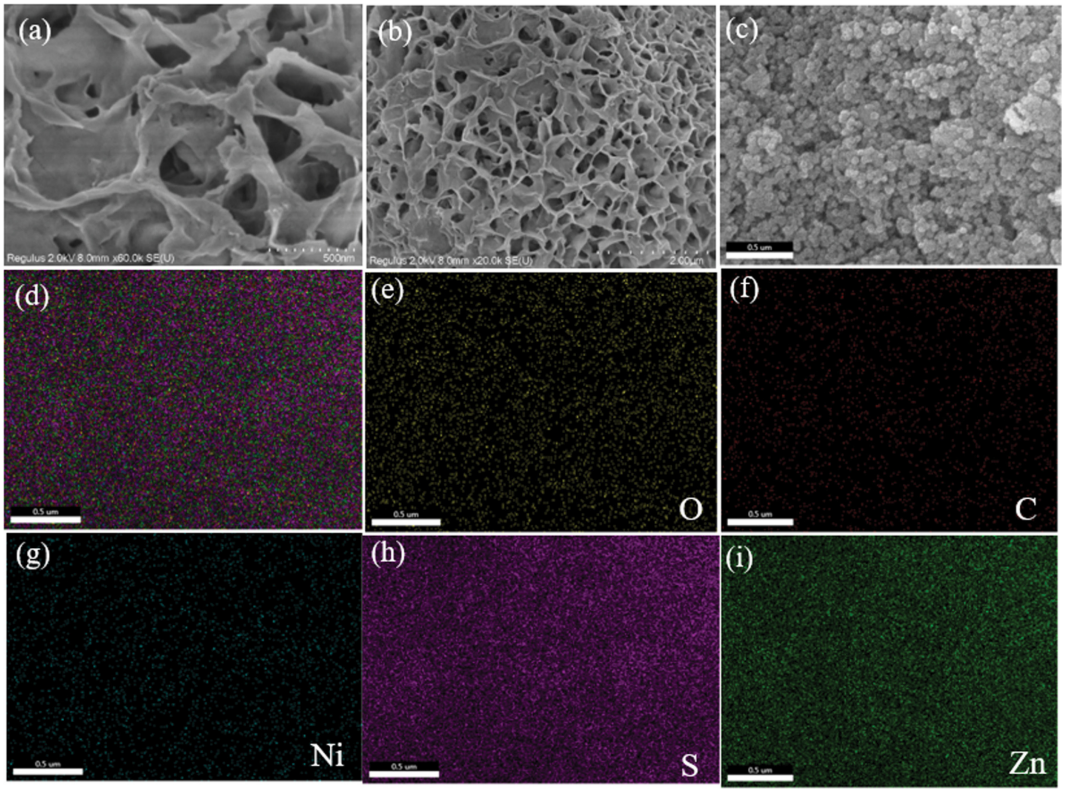


**Fig. S2. (a)-(b) SEM image of Ni-TA; (c)-(i) mapping image of 3% ZnS/Ni-TA.**